On divergent Richtmyer–Meshkov instability of a light/heavy interface

**Ming Li[1], Juchun Ding[1],†, Zhigang Zhai[1], Ting Si[1], Naian Liu[2],
Shenghong Huang[3] and Xisheng Luo[1,2],†**

[1]Advanced Propulsion Laboratory, Department of Modern Mechanics, University of Science
and Technology of China, Hefei 230026, PR China

[2]State Key Laboratory of Fire Science, University of Science and Technology of China,
Hefei 230026, PR China

[3]CAS Key Laboratory of Mechanical Behavior and Design of Materials, University of Science
and Technology of China, Hefei 230026, PR China

We report the first experiments on divergent shock-driven Richtmyer–Meshkov instability (RMI) at well-controlled single-mode interfaces. These experiments are performed in a novel divergent shock tube designed by shock dynamics theory. Generally, the perturbation growth can be divided into three successive stages: linear growth, quick reduction in growth rate and instability freeze-out. It is observed that the growth rate at each stage is far lower than its counterpart in planar or convergent geometry due to geometric divergence. We also found that nonlinearity is much weaker than that in planar or convergent RMI, and has a negligible influence on the overall amplitude growth even at late stages when it has become strong. This weak nonlinear effect is because the growth of the third harmonic counteracts its feedback to the fundamental mode. As a consequence, the linear theory of Bell (report no. LA-1321) accounting for geometric divergence and Rayleigh–Taylor (RT) stabilization caused by flow deceleration can reasonably predict the present results from early to late stages. The instability freeze-out at late times is ascribed to the negative growth induced by geometric divergence and RT stabilization, and is also well reproduced by the linear theory.

Key words: turbulent mixing, shock waves, compressible turbulence

1. Introduction

When a shock wave impinges upon a corrugated interface separating two different materials, initial perturbations on the interface grow continuously with time and, meanwhile, cause intense material mixing. This type of hydrodynamic instability is usually referred to as Richtmyer–Meshkov instability (RMI) since it was first theoretically analysed by Richtmyer (1960) and later experimentally confirmed by Meshkov (1969). The RMI is considered as an impulsive variant of Rayleigh–Taylor (RT) instability (Rayleigh 1883; Taylor 1950) that occurs at a perturbed interface under a finite and sustained acceleration. Over the past decades, the RMI has become a subject of intensive research

† Email addresses for correspondence: djc@ustc.edu.cn, xluo@ustc.edu.cn

due to its crucial role in various industrial and scientific fields such as inertial confinement fusion (ICF) (Lindl *et al.* 2014), supersonic combustion (Yang, Kubota & Zukoski 1993) and supernova explosion (Kuranz *et al.* 2018).

In terms of flow cross-section area, the RMI can be divided into two categories: area-invariant RMI and area-varied RMI. The former usually refers to the planar shock-induced RMI, which has been extensively studied through experiment, simulation and theoretical analysis and the flow regimes have been well understood (Brouillette 2002; Ranjan, Oakley & Bonazza 2011; Zhou 2017). In addition to the common flow mechanisms such as baroclinic vorticity and pressure perturbation presented in the planar RMI (Brouillette 2002; Ranjan *et al.* 2011; Zhou 2017), the area-varied case involves new physical regimes including the Bell–Plesset effect (Bell 1951; Plesset 1954) and RT stability or instability caused by flow acceleration or deceleration (Ding *et al.* 2017; Luo *et al.* 2018), and thus presents much more complicated phenomena and processes. Two simple, yet important, representatives of area-varied RMI are the convergent shock-induced RMI (convergent RMI) and the divergent shock-driven case (divergent RMI).

The convergent RMI, which possesses initial settings relevant to ICF, has attracted much attention in recent years. The first shock-tube experiment on the convergent RMI was reported in a coaxial shock tube (Hosseini, Ogawa & Takayama 2000; Hosseini & Takayama 2005) and a quicker growth of turbulent mixing zone width than the planar counterpart was observed. Later, the evolution of polygonal and single-mode interfaces impacted by a cylindrical shock was examined with high-speed laser sheet imaging in a similar shock tube (Si *et al.* 2015; Lei *et al.* 2017). Based on shock dynamics theory, a convergent shock tube with a special wall profile which can smoothly convert a planar incident shock into a perfect cylindrical one was designed and manufactured (Zhai *et al.* 2010). Subsequently, evolutions of various distorted interfaces accelerated by a cylindrical shock were examined in this facility (Si, Zhai & Luo 2014; Luo *et al.* 2018). The convergent RMI at a single-mode heavy/light interface was realized by a gas lens technique which was originally proposed by Dimotakis & Samtaney (2006) and later extended by Vandenboomgaerde & Aymard (2011), and the experimental results exhibited great potential for studying the convergent RMI (Biamino *et al.* 2015). It was observed that the perturbation amplitude presents a long-term linear growth with time, which was later carefully explained by Vandenboomgaerde *et al.* (2018) through theoretical analysis and numerical simulation. Recently, the growth of a sinusoidal air–SF_6 interface subjected to a cylindrically convergent shock was measured in a semiannular shock tube (Luo *et al.* 2015; Ding *et al.* 2017), and the influences of the geometric convergence and RT stability on the perturbation growth were first quantified in experiments. The above studies demonstrated that the contraction of the flow cross-section brings additional physical regimes and hence greatly affects the instability growth.

Compared with the convergent RMI, the divergent counterpart has received much less attention although it is equally important in nature and applications. For example, it is a dominant hydrodynamic instability in core-collapse supernova explosion (Arnett *et al.* 1989; Kuranz *et al.* 2018). The divergent RMI also occurs inevitably in the reshock process of the convergent RMI and greatly enhances the material mixing. However, the divergent RMI cannot be simply treated as an opposite of the convergent case, i.e. cannot be simply understood by replacing opposite geometric effects in the convergent RMI, because the flow features of the former as well as the behaviours of nonlinearity and compressibility may be completely different from the latter. So far, there is a substantial lack of experimental study on the divergent RMI, which is mainly ascribed to the great

difficulties in producing an initially controllable divergent shock. The existing methods for producing divergent shocks (essentially they are blast waves), mainly including making explosion at the apex of a conical tube (Stewart & Pecora 2015) and letting a shock wave expand in free air (Chandra *et al.* 2012), introduce complex physical processes and many interference factors, and hence the divergent shock formed is uncontrollable. Moreover, for divergent RMI experiments, the experimental facility and method should satisfy additional requirements for creating an idealized material interface, which brings challenges as well. These motivate the current study.

In this work, we propose a new idea for generating a controllable divergent shock: first concentrate the flow energy at a small local region and then release the energy to produce a uniform divergent shock. For this purpose, a novel divergent shock tube is designed based on shock dynamics theory. Specifically, a smooth convergent–planar–divergent shock transformation is built, which first converts a planar incident shock into a cylindrically convergent one, then intensifies the cylindrical shock through shock convergence (energy concentration) and finally produces a perfect divergent shock. Therefore, perfect cylindrical shocks, free of disturbing waves, can be obtained and the shock strength and shape (e.g. divergent angle) can be easily controlled. Also, an advanced soap film technique is realized to produce well-characterized single-mode interfaces. With these efforts on making perfect initial conditions, we can elaborately examine the divergent RMI. The perturbation growth for the evolution of a single-mode interface will be measured for the first time. The effects of geometric divergence, RT stability and nonlinearity on the perturbation growth can then be clarified.

2. Experimental methods

The experiments are conducted in a divergent shock tube designed by shock dynamics theory. A sketch of the curved part of the shock tube executing the planar–convergent–planar–divergent shock transformations is shown in figure 1(*a*) (not drawn to scale). This curved part has a length of approximately 2.1 m and an inner height of 7.0 mm. The left-hand end of this part is connected to the driven and driver sections, and the whole shock tube has a length of 6.4 m. In experiments, a planar shock wave with a Mach number of 1.35 is first generated by suddenly releasing the high-pressure gas in the driver section. When this planar shock propagates on the concave wall AB (A_1B_1), it is gradually transformed to a cylindrical one. As time proceeds, the cylindrical shock converges along the oblique wall BC (B_1C_1) with its strength being progressively augmented. Afterwards, the intensified cylindrical shock is converted back into a planar one by a convex wall CD (C_1D_1). The planar shock formed here (Mach number 1.71) is much stronger than the original one due to the large shrink in shock front (Zhan *et al.* 2018). As this planar shock travels on the second concave wall EF (E_1F_1), it is gradually converted to a cylindrically divergent shock. Later, this divergent shock moves outwards and impacts the downstream single-mode air–SF_6 interface, initiating the divergent RMI. The design principle for the curved walls (AB, A_1B_1, CD and C_1D_1) executing planar–converging–planar shock transformation has been detailed and validated in previous works focusing on the shock propagation and shock enhancement (Zhai *et al.* 2010; Zhan *et al.* 2018), and thus is not repeated here.

In this work, we generalize the same principle to the design of the concave wall EF (E_1F_1) which executes the planar–divergent shock transformation. A brief introduction of the design process is given below. Based on the shock dynamics theory, when a planar shock wave moves along a curved wall, disturbances produced from the shock foot propagate along the shock front and then gradually change the shock shape and strength.
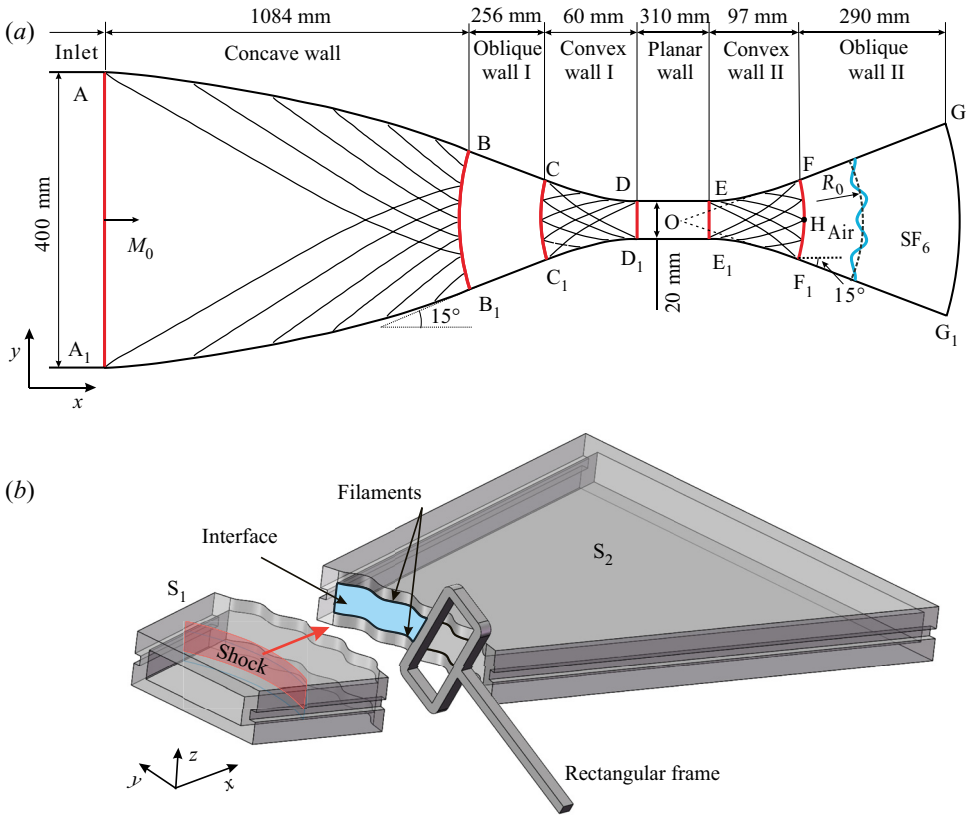
FIGURE 1. Sketches of (*a*) the divergent shock tube and (*b*) the interface formation by a soap film technique. The filaments are of a sinusoidal shape aiming to constraint the soap film such that a sinusoidally shaped soap film can be formed.

Here, we solve an inverse problem. Assuming a perfect cylindrical divergent shock produced at FH (H is the central point of FF_1), given the Mach number (M_E) of the planar shock propagating along DE, the height of DD_1 and the diverging angle ($\theta_o = 15°$ in this work), the curved wall profile EF can be calculated according to shock dynamics theory. The first step is to determine the position of point F. In order to ensure that the cylindrical shock diverges along FG, the ray angle of point F (which is defined as the angle between the moving direction of the shock front at this point and the horizontal axis) should equal the diverging angle θ_o. According to the characteristics and characteristic relations, the ray angle of point F can be expressed as

$$\theta_F = \theta_o = \int_{M_E}^{M_F} \frac{\mathrm{d}M}{cA_c}, \tag{2.1}$$

where c is the speed of the nonlinear disturbance wave, A_c is the cross-sectional area of the flow, M is the shock Mach number and

$$cA_c = \sqrt{(M^2 - 1)K(M)/2}, \tag{2.2}$$

where

$$K(M) = \left[\left(1 + \frac{2}{\gamma + 1} \frac{1 - \sigma^2}{\sigma} \right) \frac{2\sigma + 1 + M^{-2}}{2} \right]^{-1}, \tag{2.3}$$

with

$$\sigma = \sqrt{[(\gamma - 1)M^2 + 2]/[2\gamma M^2 - (\gamma - 1)]}, \tag{2.4}$$

where γ is the specific heat ratio of the gas. Based on (2.1), the Mach number of the cylindrical shock FH can be calculated. Then, according to the Chester–Chisnell–Whitham (known as CCW) relation (Chester 1954; Chisnell 1957; Whitham 1958), the area of the cylindrical shock front FH can be estimated by

$$\frac{2M \, dM}{(M^2 - 1)K(M)} + \frac{dA_c}{A_c} = 0. \tag{2.5}$$

Considering that point F is located at the straight line FG, the coordinates of point F can be readily obtained. If we discretize the curve FH into many small equal parts, the Mach number and the ray angle of any points on FH are known. Then, we can use the method of characteristics to calculate the parameters of arbitrary points in the double-wave and single-wave regions, successively. Finally, the curved profile EF is obtained. For more details, the reader is referred to Zhai *et al.* (2010).

A novel soap film technique, which has been developed recently to generate well-defined gas interfaces free of short-wavelength perturbations, diffusion layer and three-dimensionality in a planar geometry (Liu *et al.* 2018), is extended to the present divergent test section. As illustrated in figure 1(*b*), two transparent devices S_1 and S_2 (made by a 3.0 mm thick acrylic plate) whose connecting boundaries possess a sinusoidal shape, are manufactured by a high-precision engraving machine. Each device has a trapezoidal cross-section ($x-y$ plane) and two sinusoidal grooves (1.0 mm in thickness and 0.5 mm in width) are manufactured on the internal sides of its upper and lower plates, respectively. Then two thin filaments (0.75 mm in thickness and 0.5 mm in width) with the same sinusoidal profile are mounted into the grooves of the upper and lower plates, respectively, to produce the desired constraints. Note that the protrusion height of each filament into the tube is less than 0.3 mm, such that the filaments have a negligible influence on the flow field. As a rectangular frame dipped with soap solution (60 % distilled water, 20 % sodium oleate and 20 % glycerine by volume) is pulled along the sinusoidal constraints, a sinusoidally shaped soap film is immediately produced. Subsequently, the long device S_2 with a soap film on its boundary is gently inserted into the test section until it is in full contact with the short device S_1 which is placed at the test section in advance. To generate an air–SF_6 interface, SF_6 is slowly injected to the test section to gradually exhaust the air on the right-hand side of the interface. Note that a high concentration of SF_6 (measured by a gas concentration detector) is attained for each experimental run (above 90 % in mass fraction), which ensures repeatable initial conditions. It is worth mentioning that the present initial conditions including the shock profile, intensity and the interface shape can be well controlled, which enables a careful examination of the divergent RMI.

In a cylindrical coordinate system, a single-mode interface can be parameterized as $r(\theta) = R_0 + a_0 \cos(n\theta)$, where R_0 stands for the radius of initial interface, a_0 for the initial amplitude, n for the azimuthal mode number and θ for the azimuthal angle. For the present experiments, $R_0 = 130$ mm is adopted, and the strength of the incident divergent shock is Ma $= 1.27 \pm 0.02$ when it meets the initial interface. The shock-interface interaction is recorded by a high-speed schlieren system composed of a high-speed video camera

(FASTCAM SA5, Photron Limited), a DC regulated light source (DCR III, SCHOTT North America, Inc.) and several optical mirrors. The frame rate of the high-speed camera is set as 75 000 frames per second, with a shutter time of 1 μs. The spatial resolution of the schlieren images is $\sim$0.5 mm pixel^{-1}. The ambient pressure and temperature are 101.3 kPa and 298.5 K, respectively.

3. Results and discussion

To check the divergent shock tube and also understand the non-uniform flow feature in the divergent RMI, an undisturbed cylindrical air–SF$_6$ interface impacted by the cylindrically divergent shock is first considered. As shown in figure 2(*a*), when the incident shock, IS, strikes the undisturbed initial interface, II, it bifurcates into an outward-moving transmitted shock, TS, and an inward-moving reflected shock (not visible in schlieren images due to its very weak intensity). Here, the incident and transmitted shock fronts match well with the circular arcs (dashed lines) of the same centre, which verifies the feasibility of the present method. As time proceeds, the shocked interface, SI, moves outwards following the transmitted shock. It is seen that the wall boundary layer has a limited influence on the movement of the near-wall interface, and the whole interface maintains a nearly cylindrical shape during the experimental time. Variations of displacements of the waves and interface versus time are plotted in figure 2(*b*). After the shock impact, the interface moves outwards at a nearly constant speed of approximately 91 m s^{-1} ($t < 500$ μs) and later undergoes a noticeable deceleration, which will cause RT stability or instability for a perturbed interface (Ding *et al.* 2017). The transmitted shock also presents a distinct deceleration, which indicates a gradual attenuation of the divergent shock. Therefore, the present interface deceleration is induced by a gradually decaying divergent shock, which is quite different from the convergent case. In the convergent shock tube, the convergent shock becomes stronger with time such that the pressure behind the convergent shock becomes higher, which decelerates the interface movement. We also note that both cases are in an unsteady flow and, consequently, there are no analytic solutions. Assuming incompressible and steady subsonic flow, it can be easily found that the flow deceleration due to expansion is $\mathrm{d}v/\mathrm{d}t = -v^2/r$ at radius r and time t from the volume conservation. As compared in figure 2(*b*), the steady theory can roughly or qualitatively estimate the interface deceleration in a divergent geometry, but it overestimates the interface deceleration in experiment ($\sim$10 % at 900 μs).

For the present experiment, the length Reynolds number of the boundary layer of the air (SF$_6$) flow in the divergent test section is calculated to be 4.8×10^5 (2.8×10^6). Although this value approaches the upper limit of the critical Reynolds number of transition ($3.5 \times 10^4 \sim 5.0 \times 10^6$) (Reshotko 1976; Saric, Reed & Kerschen 2002), the boundary layer in experiment is laminar or at least not fully turbulent during the time of interest. This can be demonstrated by the schlieren images shown in figure 3 where the material interface close to the wall presents clear and ordered structures even at late stages. Hence, the post-shock boundary layer can be assumed to be laminar and incompressible, and its thickness (δ^*) can be estimated by

$$\delta^* = 1.72\sqrt{\frac{\mu x}{\rho \Delta v}}. \tag{3.1}$$

The maximum distance travelled by the interface during the experimental time is measured to be $x \approx 80$ mm. The viscosity coefficient and the density of pure air (SF$_6$) under the experimental conditions are $\mu = 1.83 \times 10^{-5}$ Pa s$(= 1.60 \times 10^{-5}$ Pa s$)$ and $\rho = 1.204$ kg m$^{-3}(= 6.143$ kg m$^{-3})$, respectively. The velocity of the post-shock flow
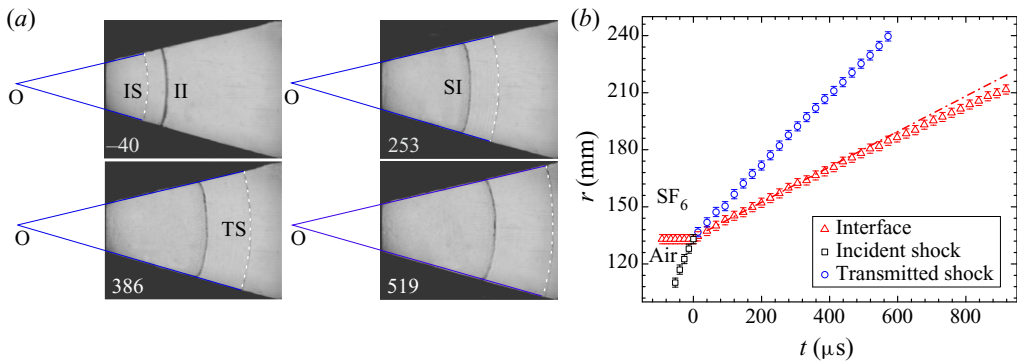
FIGURE 2. (*a*) The interaction of a divergent shock with an unperturbed air–SF$_6$ interface. The numbers have units µs. Dashed lines stand for circular arcs with the same centre as the cylindrical shock front. (*b*) Trajectories of the waves and interface. In panel (*a*): IS, incident shock; II, initial interface; SI, shocked interface; TS, transmitted shock. Dash–dotted lines represent the uniform movements of transmitted shock and shocked interface, and the solid line is the trajectory of the interface predicted by a steady theory.
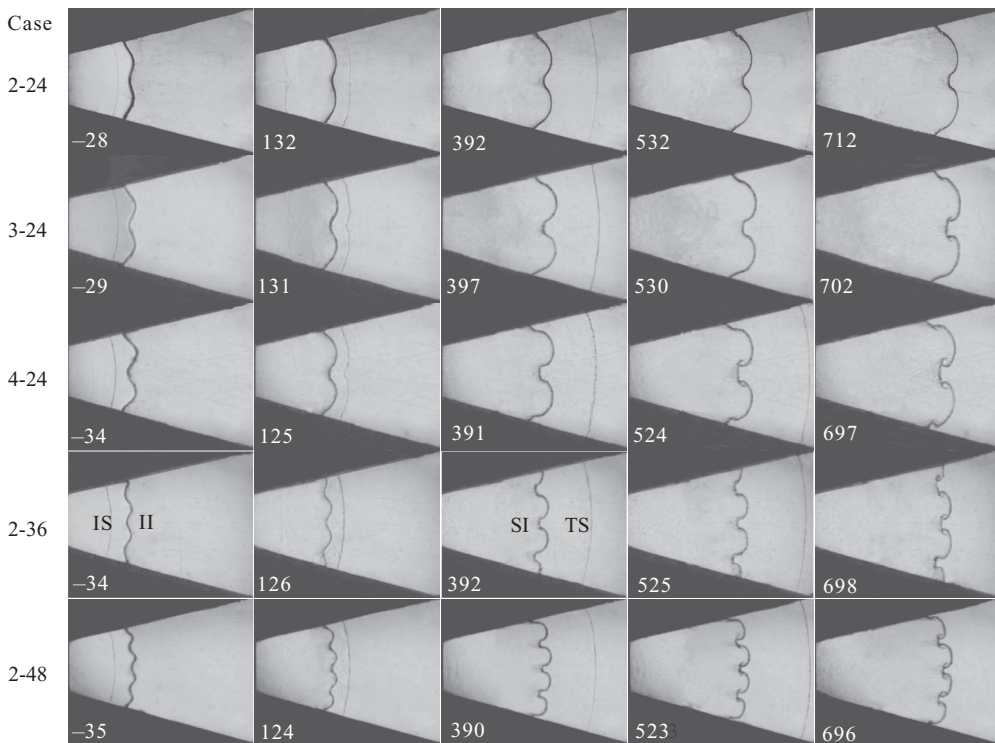

FIGURE 3. Evolution of a single-mode air–SF$_6$ interface subjected to a cylindrically exploding shock for all cases. The symbols are the same as those in figure 2. The numbers have units µs.

is $\Delta v \approx 91$ m s^{-1}. According to (3.1), the maximum thickness of the boundary layer is calculated to be approximately 0.19 mm in the air flow (0.08 mm in the SF$_6$ flow), which is much smaller than the inner height of the test section (7.0 mm). This indicates a negligible influence of the boundary layer on the interface development.

Case $(a_0 - n)$	a_0/λ	Ma	MF(SF$_6$)$_L$	MF(SF$_6$)$_R$	A	v_i (m s^{-1})	Δv (m s^{-1})	v_0 (m s^{-1})
0-0	—	1.26	0.09	0.95	0.58	413.9	91.0	—
2-24	0.058	1.26	0.09	0.96	0.60	413.6	89.4	11.0
3-24	0.088	1.28	0.09	0.95	0.59	420.7	98.1	14.1
4-24	0.117	1.27	0.09	0.94	0.59	419.8	97.4	15.4
2-36	0.088	1.25	0.05	0.94	0.59	418.6	89.2	12.0
2-48	0.117	1.28	0.09	0.94	0.58	420.2	98.5	13.3

TABLE 1. Parameters corresponding to the initial conditions for each case (denoted by $a_0 - n$) with a_0 and n being the initial amplitude and azimuthal mode number of the interface, respectively. Specially, case 0-0 denotes the unperturbed case. Here, A refers to the Atwood number, λ to the wavelength and v_0 to the amplitude growth rate at the early stage. Here, MF(SF$_6$)$_L$ and MF(SF$_6$)$_R$ denote the mass fractions of SF$_6$ on the left- and right-hand sides of the interface, respectively. The velocities of the incident shock and shocked interface are v_i and Δv, respectively.

Then, five single-mode interfaces with different amplitudes and wavelengths are considered. Detailed parameters corresponding to the initial conditions for each case (denoted by $a_0 - n$) are listed in table 1, where the Atwood number is defined as $A = (\rho_2 - \rho_1)/(\rho_2 + \rho_1)$ with ρ_1 and ρ_2 being the gas densities on the left- and right-hand sides of the interface, respectively. Specially, case 0-0 denotes the unperturbed case. Note in experiments, SF$_6$ gas could cross the soap film and contaminate the pure air on the other side of the interface. With the measured speeds of the incident shock, transmitted shock and shocked interface, mass fractions of SF$_6$ on the left- and right-hand sides of the interface can be estimated by one-dimensional gas dynamics theory. As indicated in table 1, gas contamination in the present experiments is limited and the discrepancy in Atwood number among all cases is very small.

Representative interface morphologies and wave patterns illustrating the instability development processes for five cases are displayed in figure 3. The time origin is defined as the moment when the incident shock arrives at the mean position of initial interface. Prior to shock-interface interaction, the initial interface presents a perfect single-mode shape for all cases (first column), which demonstrates the feasibility and reliability of the current experimental method. As the incident divergent shock encounters the initial interface, it splits into a corrugated transmitted shock propagating downstream and an upstream-moving reflected shock. Here, distortions on the transmitted shock decay quickly with time, which is different from the shock propagation in a convergent geometry. Later, the outgoing interface deforms continuously driven by the baroclinic vorticity deposited along it. It is observed that the present interface deformation is much slower than its counterpart in a planar or convergent geometry. This is mainly ascribed to the circumferential stretching caused by geometric expansion. Particularly, the asymmetric bubble-spike structure is not fully developed even at very late times, which indicates a very weak nonlinearity there. For cases with a larger initial amplitude-to-wavelength ratio, although the roll-up of spike appears earlier, the whole structure is also much less distorted than the planar or convergent counterpart.

Normalized variations of the perturbation amplitude with time are plotted in figure 4, where the predictions of linear and nonlinear theories are also given for comparison. The amplitude is normalized as $\alpha = n(a - a_0^+)/R_0$, and the time is scaled as
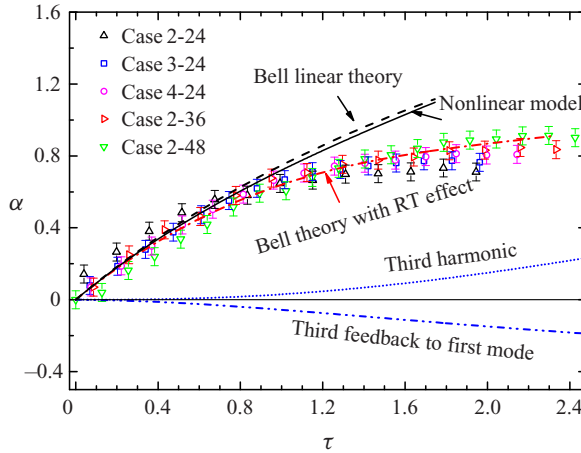
FIGURE 4. Normalized variations of the overall perturbation amplitude. The dashed (dash–dot) line denotes the linear theory of Bell (1951) without (with) the RT effect, and the solid line denotes the nonlinear theory of Wang *et al.* (2015). The dotted line refers to the growth of the third harmonic and the dash–dot–dot line to the third-order feedback to the basic mode.

$\tau = nv_0(t - t_0^+)/R_0$. Here, t_0^+ is the time just after the shock passage, a_0^+ is the post-shock amplitude and v_0 is the experimental initial growth rate. The dimensionless experimental data for all cases collapse quite well, which illustrates a universal growth behaviour of the divergent RMI. After the shock impact, the perturbation amplitude first drops suddenly to a smaller value due to shock compression, and then increases continuously in a nearly linear manner ($\tau < 0.4$). Later, the growth rate of perturbation amplitude reduces evidently. We stress that such a reduction in growth rate is mainly ascribed to the geometric divergence rather than nonlinearity, which will be addressed hereinafter. At late stages, the perturbation amplitude almost stops growing and maintains a nearly constant value. Such an instability freeze-out exists for all cases considered in this work. Therefore, we claim it is a universal phenomenon for divergent RMI.

Under the assumption of incompressible inviscid flow, Bell (1951) obtained a linear theory for the cylindrical RMI, which can be written as

$$\ddot{a} + 2\frac{\dot{R}}{R}\dot{a} - (nA - 1)\frac{\ddot{R}}{R}a = 0, \tag{3.2}$$

where $R(t)$ is the time-dependent radius of the moving interface, $\dot{R}$ ($\ddot{R}$) is the first (second) derivative of radius with time and $\dot{a}$ ($\ddot{a}$) is the first (second) derivative of perturbation amplitude with time. The development of the cylindrical RMI can be divided into two phases: the shock-driven phase (during the shock impact) and the undriven growth phase (after the shock impact). The first phase yields a post-shock growth rate of perturbation amplitude, which can be obtained by integrating equation (3.2) once from t_0 (time instant when the shock meets the interface) to t_0^+ (shortly after the shock impact). Note that during this phase, the interface is motionless, i.e. $R(t) = R_0$, and the shock impact can be approximated as an impulse function, i.e. $\ddot{R} = \delta(t)\Delta V$. Thus, the post-shock growth rate can be readily obtained as follows:

$$\dot{a}_0 = \frac{(nA - 1)\Delta V a_0^+}{R_0}. \tag{3.3}$$

Here, the post-shock amplitude a_0^+ is adopted for approximating the compressibility effect, which is similar to the treatment of Richtmyer (1960). Equation (3.3) illustrates that the cylindrical RMI possesses an initial growth rate $\dot{a}_0$ immediately after the shock impact (t_0^+). The growth rate of perturbation amplitude at an arbitrary evolution time t_1 after the shock impact can be obtained by integrating equation (3.2) from t_0^+ (with an initial growth rate $\dot{a}_0$) to t_1, which is expressed as

$$\dot{a}(t_1) = \frac{R_0^2}{R^2(t_1)}\dot{a}_0 + \frac{1}{R^2(t_1)}\int_{t_0^+}^{t_1}(nA-1)a(t)R(t)\ddot{R}(t)\,\mathrm{d}t. \tag{3.4}$$

Then, an analytical solution for the perturbation amplitude at an arbitrary time t_2 is available by integrating equation (3.4) from t_0^+ to t_2 as follows:

$$a(t_2) = a_0^+ + \dot{a}_0R_0^2\int_{t_0^+}^{t_2}\frac{1}{R^2(t_1)}\,\mathrm{d}t_1 + \int_{t_0^+}^{t_2}\left[\frac{1}{R^2(t_1)}\int_{t_0^+}^{t_1}(nA-1)a(t)R(t)\ddot{R}(t)\,\mathrm{d}t\right]\mathrm{d}t_1. \tag{3.5}$$

The second term on the right-hand side of (3.5) represents the pure RMI combined with the geometric convergence/divergence effect, and the third term denotes the RT effect caused by the flow acceleration or deceleration.

The present experimental results offer a rare opportunity to examine the validity of Bell theory for the divergent RMI. Considering that the discrepancies in the incident shock Mach number and the Atwood number among all cases in the experiments are very small, the interface trajectory for the unperturbed case (figure 2) can approximately represent the $R(t)$ for the perturbed cases. By substituting the $R(t)$ from the unperturbed case into (3.5), we can obtain the theoretical prediction of Bell theory for a perturbed case. As shown in figure 4, the Bell prediction (obtained from 3.5) assuming a steady flow (i.e. a uniform velocity of the interface) agrees reasonably with the experimental results at the early stage, but deviates later ($\tau > 0.8$). When taking the flow deceleration (indicated in the unperturbed case) into account, a good agreement between the theory and experiment is again achieved for the whole evolution process. Moreover, the instability freeze-out at late stages is also well captured by the theory. This demonstrates that the late-stage instability stagnation is mainly ascribed to the counteraction between the positive growth caused by pure RMI and the negative growth induced by geometric divergence and RT stabilization. To the authors' knowledge, this is the first direct examination of Bell theory for the divergent RMI.

To assess the nonlinearity effect, the third-order weakly nonlinear model of Wang *et al.* (2015), which assumes a small perturbation at a cylindrical interface subjected to a uniform radial motion, is employed to estimate the present perturbation growth. A brief description of this theory is given below. For the problem of two incompressible, inviscid, irrotational and immiscible fluids in an arbitrary radial motion, a velocity potential can be introduced for each fluid which satisfies the Laplace equation. Considering the kinematic and kinetic boundary conditions (i.e. the normal component of the velocity of each fluid at the interface should equal the normal velocity of the interface and also the pressure is continuous across the interface), another three governing equations for the velocity potentials can be obtained. Expanding the perturbation displacement and the velocity potentials into a power series, the first-, second- and third-order governing equations are available, and each is expressed as a second-order ordinary differential equation. Note that it is very difficult to get a general solution for the perturbation growth at a cylindrical

interface of an arbitrary implosion (explosion) history. By assuming a uniformly moving interface, the solution process is greatly simplified and the first-, second- and third-order analytical solutions can be derived. Here, we only present the first- and second-order solutions (the third-order expressions are very long and not given here),

$$a_{1,1} = a_0 + \dot{a}_0 t C_r, \tag{3.6}$$

$$a_{2,2} = a_0 \dot{a}_0 t \left(A \frac{n}{R} - \frac{1}{2} \frac{1}{R} \right) (C_r - 1) + \dot{a}_0{}^2 t^2 \left[\left(\frac{1}{6} A \frac{n}{R} - \frac{1}{4} \frac{1}{R} \right) C_r^2 - \frac{2}{3} A \frac{n}{R} C_r \right], \tag{3.7}$$

$$a_{2,0} = - \left(a_0 \dot{a}_0 t \frac{1}{2} \frac{1}{R} C_r + \dot{a}_0{}^2 t^2 \frac{1}{4} \frac{1}{R} C_r^2 \right), \tag{3.8}$$

where $C_r = R_0/R(t)$ is the convergence ratio, $a_{1,1}$ is the amplitude of the fundamental mode, $a_{2,2}$ is the amplitude of the second harmonic and $a_{2,0}$ is the second-order feedback to the zero-order mode (i.e. the radius of the unperturbed interface). For more details, the reader is referred to the original work of Wang *et al.* (2015).

As shown in figure 4, there exists only a minor difference between the linear and nonlinear predictions even at very late stages, which indicates a very weak nonlinearity for the divergent RMI. This finding is completely different from that of convergent RMI where nonlinearity is found to be strong and behaves evidently (Wang *et al.* 2015; Luo *et al.* 2019). The growth of the third harmonic together with its feedback to the primary mode, predicted by the nonlinear model of Wang *et al.* (2015), is also shown in figure 4 (the growth of the second harmonic produces no influence on the whole perturbation growth and is not given). It is found that at early stages the growth of the third harmonic in divergent geometry is much smaller than that in a planar or convergent geometry (Luo *et al.* 2019), which provides a further demonstration of weak nonlinearity. Although nonlinearity increases at late stages, the positive growth of the third harmonic approximately counteracts its negative feedback to the basic mode, which suggests a negligible influence of nonlinearity on the growth of overall perturbation amplitude. This explains well the reasonable prediction of linear Bell theory for the whole evolution process of the divergent RMI.

The high-fidelity experimental images obtained enable a reliable extraction of the interfacial contours. Taking case 3-24 as an example, interfacial profiles at seven typical time instants are extracted from schlieren images by an image processing program as shown in figure 5(*a*). By a spectrum analysis of the interfacial profiles, growths of the first, second and third harmonics are available for all cases. As shown in figure 5(*b*), the primary mode presents the same increasing tendency as the overall perturbation amplitude, i.e. first grows linearly, then slows down and eventually freezes out. Growths of the second and third harmonics are far slower, which indicates a dominant role of the primary mode at weakly nonlinear stage. The third harmonic maintains a very small amplitude during the experimental time, which implies that the energy of basic mode is mainly transferred to the second harmonic. Considerable agreement between the nonlinear prediction and the experiment for the growths of the first three harmonics is achieved for $\tau < 1.0$. Therefore, a direct validation of the nonlinear model of Wang *et al.* (2015) is performed for the divergent RMI.

In this work, the flow regimes of the divergent RMI are analysed by comparing the linear and nonlinear models (Bell 1951; Wang *et al.* 2015) with the experimental results under a limited range of initial parameters (i.e. different initial perturbation amplitudes and wavelengths under a single Mach number and Atwood). For the real ICF application, the initial conditions such as the shock Mach number, the perturbation shape and the Atwood
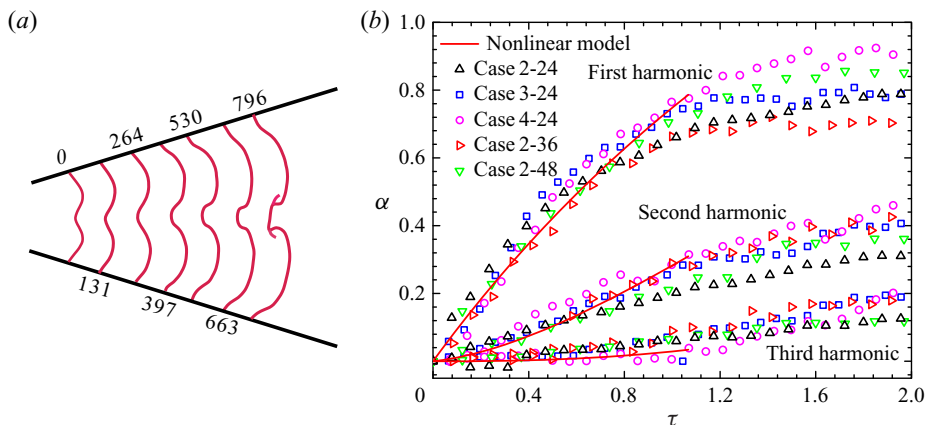
FIGURE 5. (*a*) Interfacial profiles extracted from schlieren images at seven moments (units are µs) for case 3-24. (*b*) Normalized variations of the amplitudes of the first three harmonics with time. The nonlinear model is Wang *et al.* (2015).

number are different from the present ones, and the instability growth is much more complicated. Therefore, the validity of the present model should be studied using more cases with different initial parameters including shock Mach number and Atwood number. Design and manufacture of a new divergent shock tube for generating an incident strong divergent shock is ongoing. For a very large density ratio in ICF, usually corresponding to a gas–solid interface, new interface formation methods and flow diagnostic techniques should be developed. We hope that the RMI under a strong divergent shock at a large density ratio interface can be reported in the near future.

4. Conclusions

The divergent RMI with controllable initial conditions, which is crucial for understanding hydrodynamic phenomena in ICF and supernova explosion, is studied in shock-tube experiments. A novel divergent shock tube with several curved segments transforming an incident planar shock into a perfect diverging one is designed based on shock dynamics theory and the facility is demonstrated to bring new vitality for divergent RMI study. An unperturbed case is first considered and an evident flow deceleration is observed. Then, five single-mode air–SF$_6$ interfaces with different wavelengths and amplitudes are examined. Results show that the flow structures, the instability growth behaviour and the dominant flow regimes for divergent RMI are completely different from those of convergent RMI.

Generally, the perturbation growth of divergent RMI can be divided into three successive stages: linear growth, quick reduction in growth rate and instability freeze-out. The perturbation growth in each stage is far slower than the planar or convergent counterpart due to geometric expansion. Nonlinearity in the divergent RMI is found to be much weaker than that in planar or convergent RMI. Moreover, nonlinearity in divergent RMI produces a negligible influence on the overall amplitude growth even at late stages it has become strong, which is because the growth of the third harmonic just counteracts its negative feedback to the basic mode. As a consequence, the linear theory of Bell (1951) accounting for the interface deceleration and geometric divergence can reasonably predict the present experiments from early to late stages. The instability freeze-out at late times is also well reproduced by the linear theory, which is ascribed to the counterbalancing

effect between the positive growth caused by pure RMI and the negative growth caused by geometric divergence and RT stabilization. Growths of the first three harmonics obtained by a spectrum analysis of the interfacial profiles provide a first direct validation of the nonlinear model of Wang *et al.* (2015) for divergent RMI. Despite the differences between the present experimental conditions and those of ICF, this work is the first substantial step towards the experimental study of divergent RMI. We believe that the analyses and findings of this work may provide a fundamental and important understanding of the divergent RMI, and would be also useful for understanding the reshock process of the convergent RMI in ICF.

Acknowledgements

Declaration of interests

The authors report no conflict of interest.

REFERENCES

ARNETT, W. D., BAHCALL, J. N., KIRSHNER, R. P. & WOOSLEY, S. E. 1989 Supernova 1987A. *Annu. Rev. Astron. Astrophys.* **27**, 629–700.

BELL, G. I. 1951 Taylor instability on cylinders and spheres in the small amplitude approximation. *Report No.* LA-1321. LANL.

BIAMINO, L., JOURDAN, G., MARIANI, C., HOUAS, L., VANDENBOOMGAERDE, M. & SOUFFLAND, D. 2015 On the possibility of studying the converging Richtmyer–Meshkov instability in a conventional shock tube. *Exp. Fluids* **56** (2), 1–5.

BROUILLETTE, M. 2002 The Richtmyer–Meshkov instability. *Annu. Rev. Fluid Mech.* **34**, 445–468.

CHANDRA, N., GANPULE, S., KLEINSCHMIT, N. N., FENG, R., HOLMBERG, A. D., SUNDARAMURTHY, A., SELVAN, V. & ALAI, A. 2012 Evolution of blast wave profiles in simulated air blasts: experiment and computational modeling. *Shock Waves* **22**, 403–415.

CHESTER, W. 1954 The quasi-cylindrical shock tube. *Philos. Mag.* **45**, 1293–1301.

CHISNELL, R. F. 1957 The motion of a shock wave in a channel, with applications to cylindrical and spherical shock waves. *J. Fluid Mech.* **2**, 286–298.

DIMOTAKIS, P. E. & SAMTANEY, R. 2006 Planar shock cylindrical focusing by a perfect-gas lens. *Phys. Fluids* **18**, 031705.

DING, J., SI, T., YANG, J., LU, X., ZHAI, Z. & LUO, X. 2017 Measurement of a Richtmyer–Meshkov instability at an air-SF_6 interface in a semiannular shock tube. *Phys. Rev. Lett.* **119** (1), 014501.

HOSSEINI, S. H. R., OGAWA, T. & TAKAYAMA, K. 2000 Holographic interferometric visualization of the Richtmyer-Meshkov instability induced by cylindrical shock waves. *J. Vis.* **2** (3–4), 371–380.

HOSSEINI, S. H. R. & TAKAYAMA, K. 2005 Experimental study of Richtmyer–Meshkov instability induced by cylindrical shock waves. *Phys. Fluids* **17**, 084101.

KURANZ, C. C., PARK, H. S., HUNTINGTON, C. M., MILES, A. R., REMINGTON, B. A., PLEWA, T., TRANTHAM, M. R., ROBEY, H. F., SHVARTS, D., SHIMONY, A., et al. 2018 How high energy fluxes may affect Rayleigh–Taylor instability growth in young supernova remnants. *Nat. Commun.* **9**, 1564.

LEI, F., DING, J., SI, T., ZHAI, Z. & LUO, X. 2017 Experimental study on a sinusoidal air/SF_6 interface accelerated by a cylindrically converging shock. *J. Fluid Mech.* **826**, 819–829.

LINDL, J., LANDEN, O., EDWARDS, J., MOSES, E. & TEAM, N. 2014 Review of the national ignition campaign 2009–2012. *Phys. Plasmas* **21**, 020501.

LIU, L., LIANG, Y., DING, J., LIU, N. & LUO, X. 2018 An elaborate experiment on the single-mode Richtmyer–Meshkov instability. *J. Fluid Mech.* **853**, R2.

LUO, X., DING, J., WANG, M., ZHAI, Z. & SI, T. 2015 A semi-annular shock tube for studying cylindrically converging Richtmyer–Meshkov instability. *Phys. Fluids* **27** (9), 091702.

LUO, X., LI, M., DING, J., ZHAI, Z. & SI, T. 2019 Nonlinear behaviour of convergent Richtmyer–Meshkov instability. *J. Fluid Mech.* **877**, 130–141.

LUO, X., ZHANG, F., DING, J., SI, T., YANG, J., ZHAI, Z. & WEN, C. 2018 Long-term effect of Rayleigh–Taylor stabilization on converging Richtmyer–Meshkov instability. *J. Fluid Mech.* **849**, 231–244.

MESHKOV, E. E. 1969 Instability of the interface of two gases accelerated by a shock wave. *Fluid Dyn.* **4**, 101–104.

PLESSET, M. S. 1954 On the stability of fluid flows with spherical symmetry. *J. Appl. Phys.* **25**, 96–98.

RANJAN, D., OAKLEY, J. & BONAZZA, R. 2011 Shock-bubble interactions. *Annu. Rev. Fluid Mech.* **43**, 117–140.

RAYLEIGH, LORD 1883 Investigation of the character of the equilibrium of an incompressible heavy fluid of variable density. *Proc. London Math. Soc.* **14**, 170–177.

RESHOTKO, E. 1976 Boundary-layer stability and transition. *Annu. Rev. Fluid Mech.* **8**, 311–349.

RICHTMYER, R. D. 1960 Taylor instability in shock acceleration of compressible fluids. *Commun. Pure Appl. Math.* **13**, 297–319.

SARIC, W. S., REED, H. L. & KERSCHEN, E. J. 2002 Boundary-layer receptivity to freestream disturbances. *Annu. Rev. Fluid Mech.* **34**, 291–319.

SI, T., LONG, T., ZHAI, Z. & LUO, X. 2015 Experimental investigation of cylindrical converging shock waves interacting with a polygonal heavy gas cylinder. *J. Fluid Mech.* **784**, 225–251.

SI, T., ZHAI, Z. & LUO, X. 2014 Experimental study of Richtmyer–Meshkov instability in a cylindrical converging shock tube. *Laser Part. Beams* **32**, 343–351.

STEWART, J. B. & PECORA, C. 2015 Explosively driven air blast in a conical shock tube. *Rev. Sci. Instrum.* **86**, 035108.

TAYLOR, G. 1950 The instability of liquid surfaces when accelerated in a direction perpendicular to their planes. I. *Proc. R. Soc. Lond.* A **201**, 192–196.

VANDENBOOMGAERDE, M. & AYMARD, C. 2011 Analytical theory for planar shock focusing through perfect gas lens and shock tube experiment designs. *Phys. Fluids* **23** (1), 016101.

VANDENBOOMGAERDE, M., ROUZIER, P., SOUFFLAND, D., BIAMINO, L., JOURDAN, G., HOUAS, L. & MARIANI, C. 2018 Nonlinear growth of the converging Richtmyer–Meshkov instability in a conventional shock tube. *Phys. Rev. Fluids* **3**, 014001.

WANG, L. F., WU, J. F., GUO, H. Y., YE, W. H., LIU, J., ZHANG, W. Y. & HE, X. T. 2015 Weakly nonlinear Bell–Plesset effects for a uniformly converging cylinder. *Phys. Plasmas* **22**, 082702.

WHITHAM, G. B. 1958 On the propagation of shock waves through regions of non-uniform area or flow. *J. Fluid Mech.* **4**, 337–360.

YANG, J., KUBOTA, T. & ZUKOSKI, E. E. 1993 Application of shock-induced mixing to supersonic combustion. *AIAA J.* **31**, 854–862.

ZHAI, Z., LIU, C., QIN, F., YANG, J. & LUO, X. 2010 Generation of cylindrical converging shock waves based on shock dynamics theory. *Phys. Fluids* **22**, 041701.

ZHAN, D., LI, Z., YANG, J., ZHU, Y. & YANG, J. 2018 Note: a contraction channel design for planar shock wave enhancement. *Rev. Sci. Instrum.* **89**, 056104.

ZHOU, Y. 2017 Rayleigh–Taylor and Richtmyer–Meshkov instability induced flow, turbulence, and mixing. I. *Phys. Rep.* **720–722**, 1–136.